

AperTO - Archivio Istituzionale Open Access dell'Università di Torino

Accessibility and Dispersion of Vanadyl Sites of Vanadium Silicate-1 Nanoparticles Deposited in SBA-15

This is the author's manuscript

Original Citation:

Availability:

This version is available <http://hdl.handle.net/2318/77939> since

Terms of use:

Open Access

Anyone can freely access the full text of works made available as "Open Access". Works made available under a Creative Commons license can be used according to the terms and conditions of said license. Use of all other works requires consent of the right holder (author or publisher) if not exempted from copyright protection by the applicable law.

(Article begins on next page)



UNIVERSITÀ DEGLI STUDI DI TORINO

This is an author version of the contribution published on:

Questa è la versione dell'autore dell'opera:

[J. Phys. Chem. C 114, 2010 DOI: 10.1021/jp103794x]

The definitive version is available at:

La versione definitiva è disponibile alla URL:

<http://pubs.acs.org/journal/jpccck>

Accessibility and Dispersion of Vanadyl Sites of Vanadium Silicate-1 Nanoparticles Deposited in SBA-15

S. Zamani, M. Chiesa, V. Meynen, Y. Xiao, B. Pre'lot, J. Zajac, F. Verpoort, P. Cool, S. Van Doorslaer

Department of Physics, UniVersity of Antwerp, UniVersiteitsplein 1, B-2610 Wilrijk-Antwerp, Belgium, Dipartimento di Chimica IFM, UniVersita` di Torino and NIS, Nanostructured Interfaces and Surfaces Centre of Excellence, Via P. Giuria 7, I - 10125 Torino, Italy, Department of Chemistry, UniVersity of Antwerp, UniVersiteitsplein 1, B-2610 Wilrijk-Antwerp, Belgium, CNRS-Montpellier, UniVersity of Montpellier II, ICGM - UMR CNRS 5253, 2 Place de Bataillon, CC-1502, 34095 Montpellier, Cedex 5, France, and Department of Inorganic and Physical Chemistry, UniVersity of Ghent, Krijgslaan 281, S3, B-9000 Ghent, Belgium

Abstract

Vanadium silicalite-1 (VS-1) nanoparticles dispersed onto the mesoporous walls of SBA-15 silica have characteristics different from those of the full-grown VS-1. In particular, the vanadium-binding site differs extensively. Here, we monitor the local environment of VO^{2+} with different electron paramagnetic resonance (EPR) techniques to obtain information about the heterogeneity of the vanadyl sites, the effect of a calcination/reduction cycle, and the subsequent adsorption of $^{13}\text{CO}_2$ and NH_3 to the vanadyl sites for both full-grown VS-1 and VS1-SBA15. Furthermore, two-cycle CO_2 and NH_3 adsorption experiments were performed. While the latter showed no chemisorption of CO_2 at 373 K for both materials, clear evidence was found for ligation of CO_2 to vanadyl in full-grown VS-1 by the detection of a strong ^{13}C hyperfine value. This strong binding was not detected for the vanadyl centers in VS1-SBA15. Chemisorption of NH_3 was detected for all samples both by two-cycle adsorption experiments and by EPR.

Introduction

One of the biggest drawbacks of microporous zeolites is their limited pore size (<2 nm), which makes them poorly accessible for bulky molecules. In answer to this, a wide variety of siliceous and nonsiliceous mesoporous materials have been produced,¹⁻⁵ among which, the siliceous SBA-15 material is found to be particularly promising.⁶⁻⁸ This material has a high thermal and hydrothermal stability as compared to other mesoporous systems,⁹ and the large tailorable uniform pores (3-15 nm) facilitate the catalytic turnover of large molecules. Furthermore, the material is easy to produce from cheap silicon sources.^{3,10-14} In recent years, a more mechanically stable analogue of SBA-15, the so-called plugged hexagonal templated silica (PHTS), has been synthesized by increasing the silica/surfactant ratio during the SBA-15 synthesis.^{3,15-19} In this way, microporous amorphous nanoparticles (plugs) are created inside the mesoporous channels of SBA-15. Recently, a new PHTS-type material was developed by us whereby vanadium-activated zeolitic nanoparticles (vanadium silicalite-1 (VS-1)) are deposited inside the mesoporous channels of SBA-15 by use of a postsynthesis incipient wetness impregnation with VS-1 zeolite nanoparticles.^{25,34} The amount of plugs can be controlled, and, hence, the opening and irregularities of the pores can be tuned. Moreover, the plugs influence the adsorption and diffusion of molecules in the channels, making PHTS-type materials promising to perform controlled adsorption and/or release or catalysis.²⁰⁻²⁵ However, next to the influence of the plugs on adsorption and diffusion, the specific nature and surrounding of the active element (vanadium) in the deposited zeolitic nanoparticles is of great importance toward catalysis.

It is known that the catalytic activity of the materials prepared from zeolitic nanoparticles/precursor particles can be strongly divergent from those of the full-grown zeolite.²⁶⁻²⁹ Most catalytic studies focus on the differences in catalysis that occur due to the coexistence of zeolite-like properties with mesoporosity. However, little is known about the differences in coordination and chemical surrounding of the active elements in these types of zeolitic nanoparticles/zeolite precursor particles as compared to the full-grown zeolites.

The herein discussed PHTS-type materials with vanadium activated zeolitic nanoparticles in the mesopores of SBA-15 can be particularly useful in catalytic reactions such as selective oxidation,³⁰ oxidative dehydrogenation reactions,^{31,32} or photo-catalytic reduction.³³

To understand and fine-tune the catalytic performance in heterogeneous materials such as the PHTS-type VS1-SBA15 mentioned above, it is important to unravel the local structure of the vanadium centers, and learn about the incorporation of these metals and the differences in interactions of the vanadium in the zeolitic nanoparticles as compared to the full-grown zeolite. Next to the coordination of the active element, acid/base character,³¹ and its oxidation state, also the chemical surrounding of the active element³³ has a determining effect on the performance of the catalyst (selectivity, activity, and even stability/lifetime) due to its influence on the strength of adsorption, hydrophilicity-hydrophobicity,³⁰ etc.

Electron paramagnetic resonance (EPR) is one of the most powerful methods to obtain this information, but the method is limited to paramagnetic systems.^{35,36} In the case of vanadium-containing catalysts, this is the V(IV) state, the V(V) form being diamagnetic. This implies that one is limited to the vanadyl-containing precursor states of the catalysts before calcination whereby the vanadium centers will be oxidized. Nevertheless, valuable information can be obtained from such a study, as was shown in our extensive EPR and Raman investigation of the local VO^{2+} environment in the noncalcined VS-1 nanoparticles in SBA-15 (precursor material to the final VS1-SBA15 catalyst).³⁷ This study revealed that, in contrast to the full-grown zeolite case, the vanadyl sites in the deposited nanoparticles are highly hydrophilic and experience more structural changes upon dehydration and rehydration. Furthermore, the study showed an instability of the template, TPAOH (tetrapropylammoniumhydroxide), in the zeolitic nanoparticles. The results suggest the loss of a propyl ligand from the

TPAOH molecules present on the outer surface of the VS-1 zeolitic nanoparticles that is most probably linked to the acidification of the nano-particle solution needed to introduce these zeolitic particles in SBA-15. This finding clarifies the previously reported stop in the growth of the nanoparticles into large crystals under strong acidic conditions,³⁸ and it explains why mesoporous materials can be made with these zeolitic nanoparticles as building blocks without crystalline byproduct.³⁹ Finally, the VO^{2+} sites were found to reside on the surface of the nanoparticles, revealing also interesting information on transition-metal incorporation during zeolite growth.

In the present study, the characteristics of the vanadium sites in VS1-SBA15 are further investigated using different continuous-wave (CW) and pulsed EPR techniques and two-cycle adsorption. We focus here on the following aspects: heterogeneity and dispersion of the vanadium sites, effects of a calcinations/ reduction cycle on the vanadium sites, and the adsorption of CO_2 and NH_3 to the noncalcined samples and to samples that have gone through a calcination/reduction cycle.

Experimental Methods

Sample Preparation. The various materials were prepared as described in refs 25 and 37. A vanadium silicalite-1 (VS-1) nanoparticles suspension was prepared by dissolving tetrapropylammoniumhydroxide (TPAOH) 20% solution (Aldrich) and TEOS in water. Subsequently, the solution TPAOH:TEOS: H_2O with molar ratio 1:6.4:100 was heated to about 343 K. After evaporation of 50% of the solution, the clear solution was cooled to room temperature. Next, 0.3 g of VOSO_4 in 30 mL of water was added to about 15 mL of clear solution under vigorous stirring. Afterward, this clear solution was aged at room temperature for 5 days. The preparation of the full-grown zeolite VS-1 was identical, with the exception that the aging period was replaced by a hydrothermal treatment of 5 days at 453 K. After dilution and acidification with 0.6 M HCl to pH) 1, the clear solution of VS-1 nanoparticles was deposited by means of incipient wetness impregnation inside the calcined SBA-15 samples. This final product (hereafter named VS1-SBA15) was dried in ambient atmosphere and calcined under ambient atmosphere up to 823 K for 6 h with a heating rate of 1 K per minute.

Different samples were prepared that involved treatments of the material prior to or after the final calcination step in the synthesis of VS-1 or VS1-SBA15 as outlined in Table 1. The numbering of the materials in Table 1 will be used throughout the whole Article.

Two-Cycle Adsorption. Two-cycle adsorption experiments were done on a micrometrics ASAP 2010. Each sample was degassed prior to the measurements at 523 K for 12 h. Afterward, the sample reduction step was carried out in a flow

TABLE 1: List of the Samples Studied in This Work

number	sample description
1	noncalcined full-grown VS-1 - freshly made
2	noncalcined VS1-SBA15 - freshly made
3	sample 2, dehydrated under a dynamic vacuum of 10^{-6} mbar at 100 °C
4	sample 1 calcined and subsequently reduced under H_2 stream
5	sample 2 calcined and subsequently reduced under H_2 stream
6	sample 5 evacuated and subsequent addition of NH_3
7	sample 1 evacuated and subsequent addition of $^{13}\text{CO}_2$
8	sample 2 evacuated and subsequent addition of $^{13}\text{CO}_2$
9	sample 4 evacuated and subsequent addition of $^{13}\text{CO}_2$
10	sample 5 evacuated and subsequent addition of $^{13}\text{CO}_2$

of hydrogen at 673 K during 20 min. Finally, the sample was degassed again for 2 h at 673 K after which it was allowed to cool to 373 K in a flow of helium. The two-cycle adsorption experiments were performed under equilibrium adsorption conditions at 373 K with gaseous CO_2 and NH_3 as probe molecules for base and acid sites on the solid surface. During each experimental run, successive doses of a reactive gas (CO_2 or NH_3) were sent onto the sample until a final equilibrium pressure of about 40 Torr was reached. The equilibrium pressure was measured after each adsorption step, and the amount of CO_2 or NH_3 adsorbed was calculated. At the end of the first adsorption cycle, the sample was degassed under vacuum at 373 K for 60 min, and a second adsorption cycle was then performed at the same temperature.

EPR Spectroscopy. Prior to gas ($^{13}\text{CO}_2$ and NH_3) adsorption, the calcined samples were outgassed at 523 K under dynamic vacuum (10^{-5} mbar) and subsequently reduced in H_2 (30 mbar) at 673 K for 20 min. Twenty-five mbar of $^{13}\text{CO}_2$ and 10 mbar NH_3 were admitted in the cell at room temperature. The cell was then sealed to perform the EPR experiments.

X-band CW-EPR spectra were recorded on a Bruker ESP 300E spectrometer at ~ 9.5 GHz microwave (mw) frequency and on a Bruker ESP 380E spectrometer (working mw frequency ~ 9.7 GHz), both equipped with a gas-flow cryogenic system. The mw frequencies are given in the figure captions. A mw power of 10 mW, a modulation frequency of 100 kHz, and a modulation amplitude of 0.5 mT were applied. The CW-EPR spectra were simulated using the EasySpin program, a MAT-LAB-based simulation tool.⁴⁰

X-band pulsed EPR spectra were recorded on a Bruker ESP 380E operating at a microwave (mw) frequency of 9.7 GHz and equipped with a liquid helium cryostat (Oxford Inc.). All pulse EPR experiments were recorded with a repetition rate of 1 kHz.

2D Electron-Spin-echo (ESE) Detected EPR Spectra. The experiments were carried out with the pulse sequence: $\pi/2 - \tau - \pi - \tau$ -echo, with mw pulse lengths $t_{\pi/2}$) 16 ns and t_{π}) 32 ns and a τ value starting from 96 ns with 8 ns increment per step. The spectra were recorded in a two-dimensional way, whereby τ was stepped in one dimension and the magnetic field was swept in the other dimension from 260 to 460 mT in steps of 1 mT. The values of the phase-memory times T_m were obtained from a nonlinear least-squares fit of the peaks in the echo envelope to a mono- or biexponential curve.

TABLE 2: Spin-Hamiltonian Parameters of Vanadium-Based Centers in VS-1 and VS1-SBA15 upon Different Treatments^a

sample	g_z (0.0010)	$g_{x,y}$ (0.006)	$ A_z $ (3)	$ A_{x,y} $ (5)
1	1.9392	1.962, 1.979	513	165, 188
	1.9336	1.962, 1.979	537	165, 188
2	1.9383	1.978	537	194
3	1.9303	1.976	530	187
4	1.937	1.975, 1.969	519	190, 170
5	1.926	1.975	533	185
6	1.936	1.979	521	183
7	1.939	1.962, 1.979	510	165, 188
	1.9336	1.962, 1.979	533	165, 188
8	1.931	1.977	526	190
9	1.937	1.975, 1.969	517	190, 170
10	1.926	1.975	530	189

^a The parameters are obtained from computer simulations of the CW-EPR and ESE-detected EPR spectra. The sample numbering is explained in Table 1. The hyperfine coupling constants are expressed in MHz.

Hyperfine Sublevel Correlation (HYSCORE) Experiments.⁴¹

These were carried out with the pulse sequence $\pi/2-\tau-\pi/2-t_1-\pi-t_2-\pi/2-\tau$ -echo with mw pulse length $t_{\pi/2}$ 16 ns and t_π 16 ns. The time intervals t_1 and t_2 were varied in steps of 16 ns starting from 96 to 3288 ns. Different τ values as specified in the figure captions were chosen to avoid τ -dependent blind spots. An eight-step phase cycle was used to eliminate unwanted echoes.

Matched HYSCORE experiments⁴² have been performed with the sequence $\pi/2-\tau$ -(HTA)- $t_1-\pi-t_2$ -(HTA)- τ -echo with mw pulse length $t_{\pi/2}$ 16 ns and t_π 16 ns. The amplitude of the microwave field of the matching pulses was 15.625 MHz. The optimal length of the high turning angle (HTA) pulse was experimentally determined with a 2D three-pulse experiment whereby the pulse length of the second and third pulses was increased in steps of 8 ns starting from 8 ns.

The time traces of the HYSCORE spectra were baseline corrected with a third-order polynomial, apodized with a Hamming window, and zero filled. After two-dimensional Fourier transformation, the absolute value spectra were calculated. The spectra were added for the different τ values to eliminate blind-spot effects. The HYSCORE spectra were simulated using a program developed at the ETH Zurich.⁴³

Results

1. EPR Experiments. Heterogeneity and Dispersion of the VO(II) Sites. All EPR experiments performed in this work will be compared to the EPR data of freshly made noncalcined full-grown VS-1 (sample **1**) and freshly made noncalcined VS1-SBA15 (sample **2**). An extensive set of data on these samples was reported in our earlier work.³⁷ In short, the CW-EPR spectrum of sample **1** consists of two different contributions, typical of two square-pyramidal vanadyl sites.⁴⁴ The CW-EPR and HYSCORE spectra of sample **2** are characteristic for immobilized VO²⁺ species with equatorially coordinated -OH units (possibly stemming from H₂O or silanol), suggesting a partial hydration of the VO²⁺ ions. Evacuation of this sample at 373 K (sample **3**) resulted in the coordination of tripropylamine to the VO²⁺ center as revealed by the presence of clear HYSCORE cross peaks stemming from an equatorially ligated nitrogen interacting with the unpaired electron of the vanadyl ion.³⁷ The principal g and ⁵¹V hyperfine values are given in Table 2.

As is illustrated in Figure 1, the line width of the CW-EPR spectrum of sample **1** is much smaller than the linewidths found

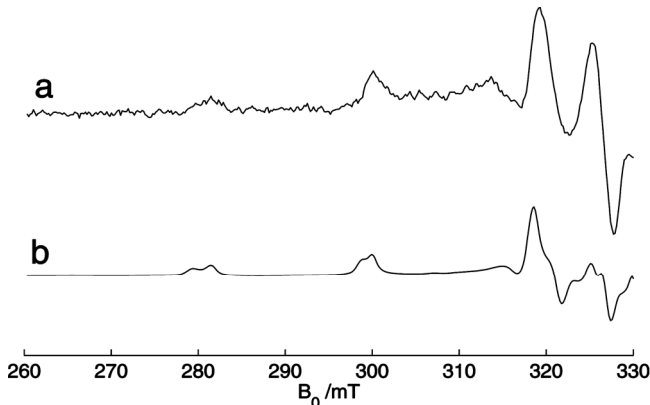


Figure 1. Details of the X-band CW-EPR spectrum of (a) sample **3** and (b) sample **1**. The difference in line width is apparent. The spectra are recorded at a mw frequency of 9.47 GHz.

for sample **3**. Similar trends were observed for **1** versus **2** (comparison not shown; for the CW-EPR spectrum of **2**, we refer to ref 37). In principle, a difference in the unresolved hyperfine couplings may explain the difference in linewidths. However, these hyperfine couplings can easily be estimated from the HYSCORE spectra³⁷ and are insufficient to account for the observed differences. An increased line width can also stem from dipolar broadening (and hence a higher local concentration of the vanadyl sites in the VS1-SBA15 samples) and/or from an increased heterogeneity in the VO²⁺ sites (different vanadyl sites with slightly different local environment and therefore slightly different EPR parameters). To check this, two-pulse ESE experiments were set up (see the Supporting Information). Despite the fact that

two VO^{2+} centers contribute to the CW-EPR spectrum (Table 2), the decay of the 2-pulse ESE time traces of sample **1** could be fitted with a monoexponential decay with phase-memory times, T_m , in the range of 310-390 ns. This indicates that the two centers distinguished in the CW-EPR spectra of sample **1** have similar relaxation characteristics and, hence, sense a similar local concentration. In contrast, the 2-pulse ESE time traces of the VS1-SBA15 samples (samples **2-3**) had to be fit with a biexponential with a dominant contribution of a short T_m value in the order of 500-1100 ns and a smaller fraction of a long T_m value in the order of 4-11 μs . Because the overall shortest T_m values are obtained for the zeolite samples, these samples have a higher local concentration of paramagnetic centers than the VS1-SBA15 samples **2** and **3**. This is in good agreement with previous reported data obtained with N_2 -sorption, HRTEM, ED, and HAADF STEM, which indicated that the VS-1 nanoparticles (estimated dimensions of 4 nm) were deposited in distinct areas of the mesopores, therefore spatially separating the nanoparticles and vanadyl centers.²⁵ The broader CW-EPR line width in the VS1-SBA15 cases thus stems from a larger heterogeneity in the vanadyl sites and not from a higher local concentration of the vanadyl sites than found for the full-grown VS-1 zeolite. This heterogeneity is also corroborated by the biexponential spin-echo decay observed for **2** and **3** and by an increased g and A strain observed for these samples.

Calcination/Reduction Cycle. Samples **4** and **5**, obtained after calcination of the samples **1** and **2** and subsequent reduction with H_2 , both exhibit a CW-EPR spectrum typical for square-pyramidal V(IV) sites as opposed to tetrahedral sites (Figure 2, Table 2). The clear difference in the EPR parameters of samples **4** and **5** indicates a marked difference in the local surrounding of the V(IV) centers in the two cases. Although two types of isolated VO(II) sites were found for sample **1**, only one V(IV) site is left after the calcination/reduction cycle (sample **4**, Table 2).

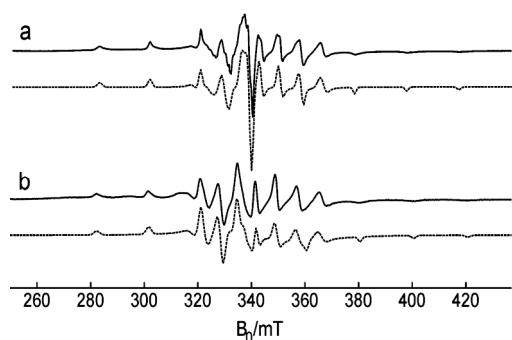


Figure 2. Comparison of the X-band CW-EPR spectra of (a) sample **4** and (b) sample **5**. Top, experimental spectra; bottom, simulations using the parameters in Table 2. All spectra were recorded at 15 K and with a mw frequency of 9.50 GHz, and the same recording conditions were taken. The spectra were then normalized.

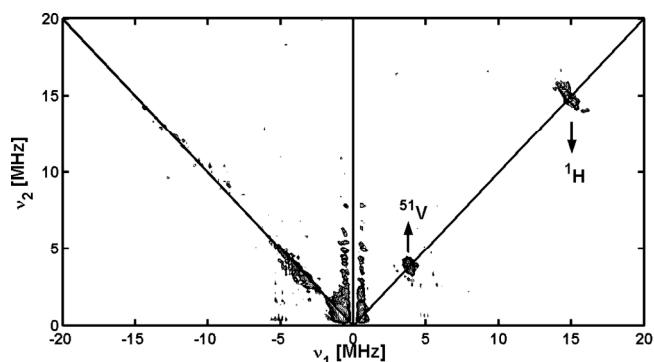


Figure 3. Experimental X-band HYSCORE spectrum of sample **5** recorded at 4 K. The spectrum was taken at $B_0 = 347.6$ mT with $\tau = 96$ ns.

The HYSCORE spectrum of sample **5** shows a very weak proton ridge in the (+,+) quadrant (maximum width of ~ 1.5 MHz) (Figure 3). The maximum proton hyperfine coupling observed for sample **5** is much smaller than earlier observed for **1-3**.³⁷ This agrees with the calcination procedure preceding the reduction process. During calcination, all water and organic ligands will be removed, and condensation reactions will take place. Hence, the only proton source will come from the H_2 stream and isolated Si-OH sites. Furthermore, a small ridge stemming from interactions with ^{51}V nuclei is observed in the HYSCORE spectra of sample **5** (Figure 3). These peaks arise from nearby V(V) ions. The reduction process was stopped in an early phase, so that many V(V) centers will be left. Note that somewhat higher proton hyperfine couplings (maximum coupling ~ 3.5 MHz) were observed for sample **4** (Supporting Information), which agrees with the difference in the g and ^{51}V hyperfine parameters for samples **4** and **5** (Table 2). Nevertheless, the magnitude of the proton interaction is in both cases smaller than the ones usually found for protons of equatorially or axially bound water or -OH protons⁴⁵ and thus stems from far away (remote) protons.

Binding of NH_3 . The local structure of the active species is key in influencing the accessibility and the subsequent reactivity of incoming molecules. NH_3 is a prototype of a Lewis base and a crucial actor in several important catalytic reactions. An earlier ESEEM study showed that the vanadyl centers of dehydrated VS-1 axially bind one ammonia molecule.⁴⁴ In contrast, vanadium-exchanged ZSM-5 zeolite treated with ammonia gives rise to equatorial NH_3 ligation to the VO(II) ion.⁴⁶

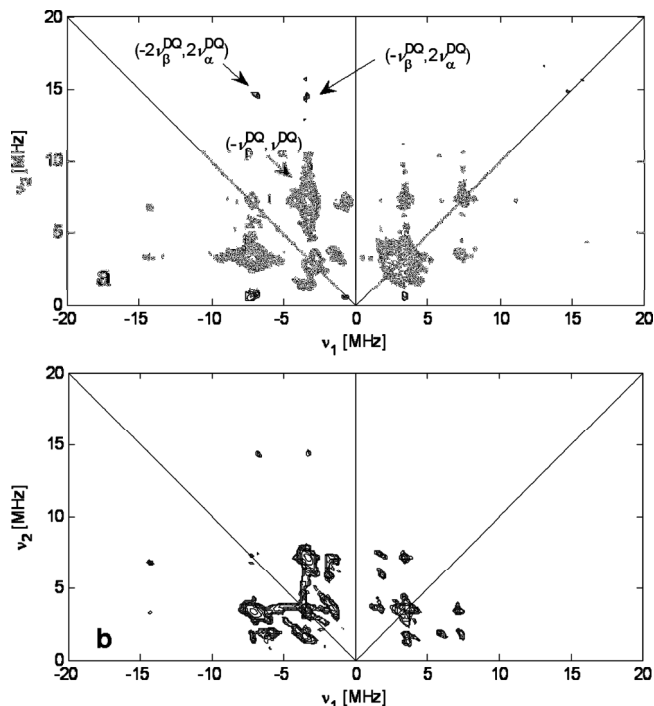


Figure 4. (a) Experimental matched HYSORE spectrum of sample **6** taken at 4 K at B_0) 347.6 mT with τ) 192 ns. The HTA pulse was 24 ns. (b) Simulation of (a).

In the latter case, the vanadium loading of the zeolite is obtained by stirring overnight a Na ZSM-5 zeolite with an aqueous solution of VO_2SO_4 . The nature of this treatment already implies that the centers are vanadyl-based as opposed to V(IV)-based and that the VO(II) centers will be highly accessible.

In the following, we check whether the vanadium sites in VS1-SBA15 are still accessible to ammonia after a calcination/ reduction cycle. NH_3 was therefore adsorbed onto sample **5** (hereafter indicated as sample **6**). The CW-EPR spectrum of sample **6** is clearly different from the one of sample **5** (Table 2, compare Figure 2b with Figure S4 (Supporting Information)). In particular, the reduction of the ^{51}V hyperfine interaction is accompanied by a shift of the isotropic g factor toward higher values. This is in line with the empirical correlation between g_z and A_z ,⁴⁷ which shows that both values decrease with increasing in-plane ligand-field strength. This trend is indicative of NH_3 binding to the V(IV) centers, and the values are consistent with those reported for ammonia adsorption on VO-ZSM-5.⁴⁶ They differ, however, from the ones reported for ammonia binding to dehydrated VS-1 (g_z) 1.935, A_z) 540 MHz).⁴⁴

The small changes in the CW-EPR experiment observed upon NH_3 adsorption to sample **5** correspond to major changes in the HYSORE spectra. Figure 4a shows the matched HYSORE spectrum from sample **6** taken at an observer position known to excite all molecular orientations. We see a clear difference with the HYSORE spectrum depicted in Figure 3. The strong features marked as $(-\nu_{\beta}^{\text{DQ}}, \nu_{\beta}^{\text{DQ}})$ are the cross-peaks between the double quantum (DQ) nuclear frequencies ($|\Delta M_I| = 2$) stemming from interactions with nitrogen nuclei. Figure 4b shows the simulation of the HYSORE spectrum with the parameters given in Table 3. The hyperfine and nuclear-quadrupole values are typical for an equatorial ligation of a nitrogen base, which is NH_3 in this case. The observation of the $(-2\nu_{\beta}^{\text{DQ}}, 2\nu_{\beta}^{\text{DQ}})$ peak indicates that we have at least two such equatorial nitrogens, or, in other words, at least two NH_3

TABLE 3: ^{14}N Hyperfine and Nuclear Quadrupole Values of Samples 3 and 6 in Comparison with Literature Results for Different Complexes Containing Amine Ligands on Vanadyls Are Also Reported for the Sake of Comparison^a

sample	$ ^N a_{\text{iso}} $ [MHz]	$ ^N A_z $ [MHz]	$ ^N A_x $ [MHz]	$ ^N A_y $ [MHz]	θ [deg]	$e^2 q Q/h$ [MHz]	η	ref
3	4.24	5.5	3.3	3.9	30	2.8	0.6	37
6	4.86 (0.05)	5.60 (0.05)	4.40 (0.05)	4.60 (0.05)	30 (5)	2.5 (0.1)	0.5 (0.1)	this work
	4.73 (0.05)	5.60 (0.05)	4.00 (0.05)	4.60 (0.05)	0 (5)	2.5 (0.1)	0.3 (0.1)	
VO(edda)	4.98	5.10	5.10	4.75		3.1	0.48	50
VO(gly) ₂	5.1	5.4	5.20	4.70		2.7	0.48	50
V-ZSM5 treated with NH_3	4.8					2-2.32	1-0	46

^a Abbreviations: H₂edda) ethylenediamine- N,N' -diacetic acid, gly⁻) glycinate; the rotation of the hyperfine versus the g tensor is assumed. represents the rotation around the y axis. Because the g tensors are axial, no information about the Euler angle a can be obtained from the spectra.

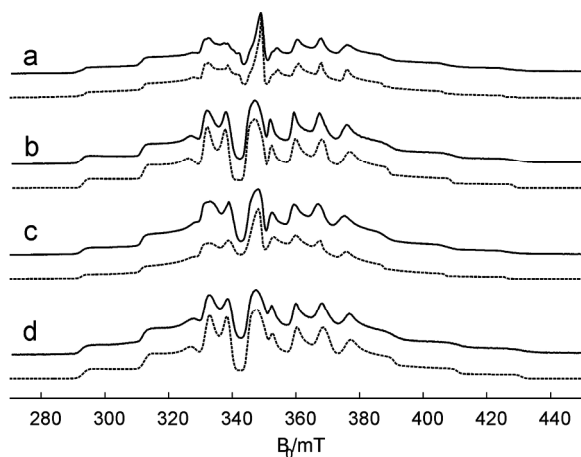


Figure 5. Comparison of the X-band ESE-detected EPR spectra of (a) sample **7**, (b) sample **8**, (c) sample **9**, and (d) sample **10**. Solid lines, experimental spectra; dashed lines, simulations using the parameters in Table 2. All spectra were recorded at 15 K, and the same recording conditions were taken. The spectra were then normalized.

molecules are binding to the vanadium ion. The HYSORE spectrum shows similarities to the one of the highly accessible VO(II) site in vanadium-exchanged ZSM-5 zeolite treated with ammonia.⁴⁶ Although the incorporation of vanadium in the zeolite nanoparticles occurred during synthesis in the case of sample **6**, the vanadium ions are located at highly accessible position on the silicate. This coincides with our earlier results,³⁷ which suggested that the vanadyl sites are located on the external surface of the VS-1 nanoparticles impregnated in the SBA-15 mesopores.

The proton modulations are largely suppressed by the strong ^{14}N modulations. In the Supporting Information (Figure S5), the proton region of Figure 4a is plotted with much lower contour levels, showing the low-intensity proton ridges stemming from the ammonia protons.

Binding of $^{13}\text{CO}_2$. As a complement to the NH_3 adsorption, we studied the coordination of a prototypical Lewis acidic molecule, carbon dioxide. $^{13}\text{CO}_2$ was thus adsorbed on the noncalcined samples **1** and **2** and the calcined/reduced samples **4** and **5** leading to materials **7-10**, respectively. Figure 5 shows the ESE-detected EPR spectra of **7-10** with their accompanying simulation using the EPR parameters given in Table 2. The corresponding CW-EPR spectra are shown in the Supporting Information (Figures S6-S9). The CW-EPR spectra do not change markedly upon $^{13}\text{CO}_2$ adsorption. Interaction of the gas molecule with the V(IV) centers is, however, clearly revealed by the HYSORE experiments (Figure 6).

Figure 6a shows the X-band HYSORE spectrum of sample **7** (dehydrated (evacuated) sample **1** with subsequent addition of $^{13}\text{CO}_2$) taken at an observer position that is known to excite all molecular orientations. No ^{13}C signals can be observed, and the spectrum is identical to the one observed for dehydrated noncalcined full-grown VS-1 (Figure 6b in ref 37). Similarly, the corresponding X-band HYSORE spectrum of sample **8** (sample **2** evacuated and subsequently treated with $^{13}\text{CO}_2$) shows no ^{13}C contribution (Figure 6c). It exhibits the characteristic ^{14}N cross peaks due to the interaction of the unpaired electron with the template nitrogen. Template coordination to the vanadyl ion was found to occur upon evacuation of **2** (compare also with Figure 4c in ref 37). The lack of CO_2 binding to vanadyl in **7** and **8** can be easily understood. The template molecules still present in the noncalcined full-grown VS-1 will block the zeolite pores, preventing CO_2 binding to the VO(II) centers inside the zeolite. In the case of VS1-SBA15, the vanadyl centers are located at the surface of the nanoparticles and bind to tripropylamine.³⁷ The weak ligand, CO_2 , is not capable of replacing this amine.

Figure 6b shows the X-band HYSORE spectrum of sample **9** (addition of $^{13}\text{CO}_2$ to sample **4**). The calcination step has now removed all template molecules, leaving a zeolite structure that should be accessible to CO_2 molecules. Indeed, two sets of ^{13}C cross-peaks marked as C(1) and C(2) are visible in the HYSORE spectrum. Figure 7a shows the simulations of these contributions using the ^{13}C hyperfine values given in Table 4. The large magnitude of the ^{13}C hyperfine values suggests direct ligation of CO_2 molecule to the vanadyl center. Furthermore, a strong signal due to a hyperfine interaction with a proton is observed. The hyperfine parameters (A) $[-0.6 -0.6 5.5]$ $[(0.5)$ MHz) are typical of an axial -OH proton.⁴⁸

Surprisingly, only one weak ^{13}C interaction could be observed in the HYSORE spectrum of sample **10** (Figure 6d). This C(1)-like contribution is partially masked by the ^{51}V signal stemming from the nearby V(V) centers (A) $[(2.4 - 0.5 - 0.5]$ $[(0.5)$ MHz). ^{51}V HYSORE signals were already present prior to CO_2 addition (Figure 3). Figure 7b shows the simulation of the ^{13}C and ^{51}V HYSORE cross peaks in Figure 6d. C(2)-like features are fully missing from the (-,+) quadrant of the HYSORE spectrum. Since it has been reported that the ESEEM contributions of weakly modulated nuclei can be suppressed by the strong modulations of other nuclei,⁴⁹ additional ENDOR (electron nuclear double resonance) experiments were performed, but no C(2)-like coupling could be revealed (not shown). Finally, a weak ^1H HYSORE ridge is observed. This signal is much lower in relative intensity than the one observed for sample **9** (compare with Figure 6b), but has a somewhat larger extension (~ 8 MHz). This may point to the presence of equatorially bound -OH groups.⁴⁸ Because of the low intensity of this signal, a full simulation of this ridge was not attempted.

2. Two-Cycle Adsorption. Because the EPR experiments only probe the local environment of the vanadyl centers, two-

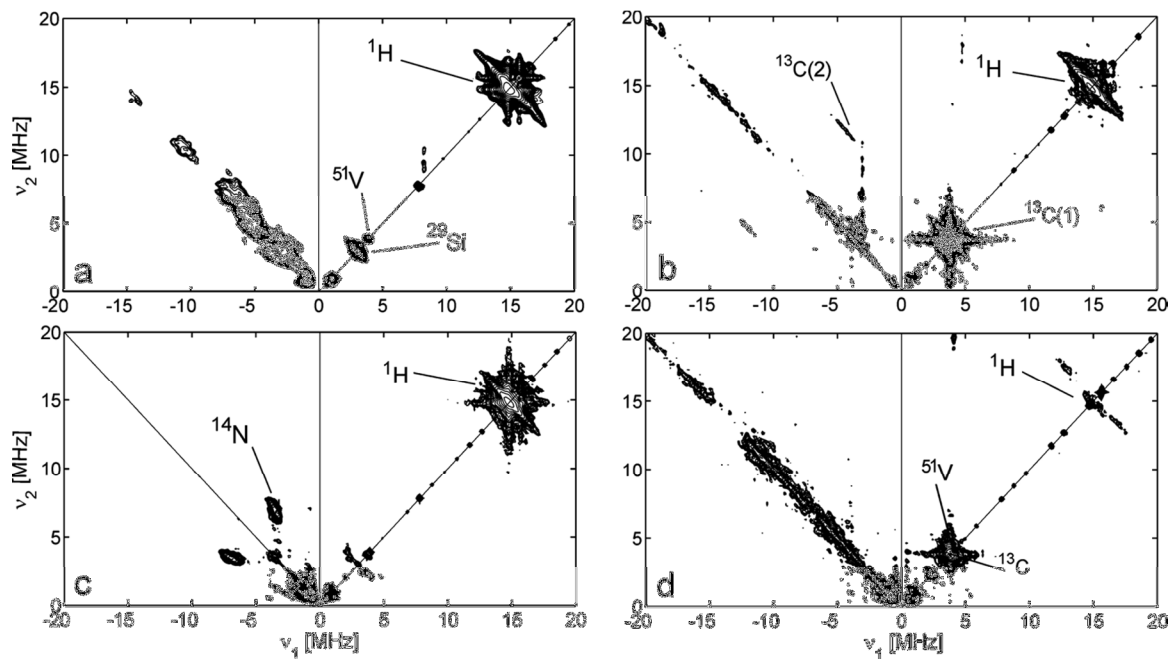


Figure 6. Experimental X-band HYSCORE spectra of (a) sample 7, (b) sample 9, (c) sample 8, and (d) sample 10. The HYSCORE spectra were measured with τ 96, 176 ns and added together. All spectra were recorded at 4 K and B_0 348.1 mT.

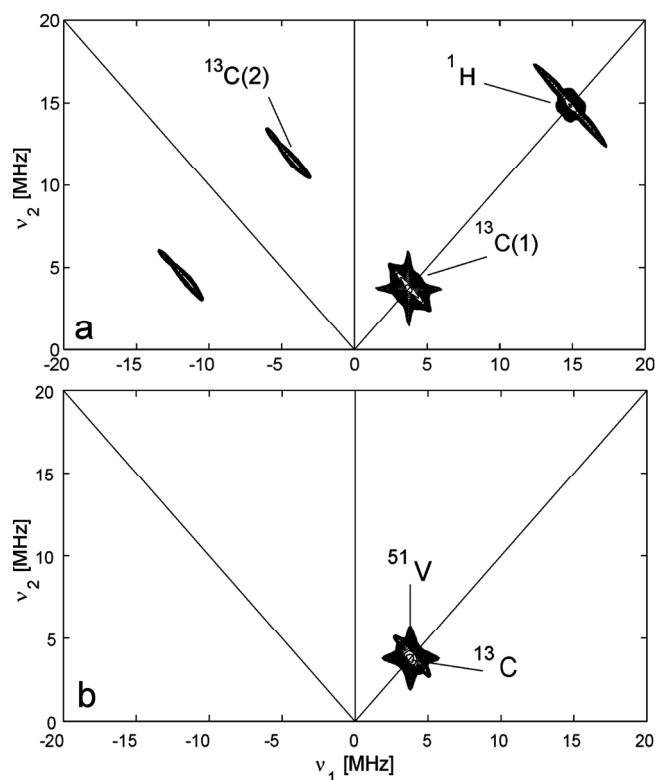


Figure 7. Simulation of the HYSORE spectra in Figure 6b and d, respectively.

cycle adsorption experiments were executed to determine the overall strength and degree of chemisorption of CO₂ and NH₃ on the support and the active vanadium sites. The measurements were done at a constant temperature of 373 K to diminish the physisorption of the probe molecules (CO₂ or NH₃). During the first adsorption cycle, both chemisorption and physisorption took place. Next, the desorption step under “mild conditions” (i.e., the same temperature, pumping only for 60 min) was pro-grammed to remove only those probe molecules that had been previously physisorbed. During the second adsorption cycle

TABLE 4: ¹³C Hyperfine Values of Samples 9 and 10 Derived by Simulation of the HYSORE Spectra in Figures 6b and d^a

sample	A ₁	A ₂	A ₃
9 C(2)	((13.0 (0.5)	((16.0(3)	((20(1)
9 C(1)	((3 (0.5)	-(0.2(0.2)	-(0.2(0.2)
10	((1.5 (0.3)	-(0.5(0.3)	-(0.5(0.3)

^a The hyperfine coupling constants are expressed in MHz.

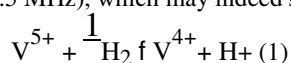
carried out at the same temperature and for the same equilibrium pressures, the amounts of the reactive gas adsorbed only through physical interactions with the surface were determined. The difference in the quantity of adsorption between the two cycles at a given equilibrium pressure could be thus ascribed to the irreversible adsorption (chemisorption) of the probe molecule under the experimental conditions applied.

Two-cycle adsorption measurements were performed on samples 4 and 5 with CO₂ as the probe molecule (Figure S10 of Supporting Information). The absence of a noticeable CO₂ uptake in the low pressure region and the linearity of the adsorption curves in the whole range studied for both samples (4 and 5) suggests a very weak chemical affinity of the material for CO₂ (i.e., very low propensity to form chemical bonds between the adsorbate and the adsorbent and/or very small number of surface sites reactive toward CO₂). Moreover, both the first and the second adsorption curves superimpose in the case of each sample. These features indicate that there is no detectable covalent bonding of V (IV and V) or the silica support with CO₂ under the experimental conditions of the two-cycle adsorption experiment, which is in good agreement with previous literature studies on MFI zeolites.⁵⁵ However, this observation is in contrast to the observed ligation of CO₂ to the vanadyl in samples 4 and 5, as seen in the EPR experiments. This could be explained by the large temperature difference applied in both techniques (373 K in two-cycle adsorption and 4 K in EPR) as covalent bond-induced adsorption will be more likely at the very low temperature applied in EPR. Similar experiments were performed on samples 4 and 5 using NH₃ as a probe molecule (Figure S11). Both samples 4 and 5 show a type II isotherm in the case of NH₃ adsorption in the first as well as the second adsorption cycle. The isotherm is concave to the pressure axis at low pressures and then almost linear at higher pressures. The shape of the isotherms is evidence for the stronger interaction of NH₃ with the surface and vanadium sites in contrast to the interaction with

CO₂. Moreover there is clearly less NH₃ adsorbed in the second adsorption cycle as compared to the first one on both of the samples. This difference in the amount adsorbed is representative for the chemisorption of NH₃ molecules, in line with the strong covalent bonding as also observed in the EPR experiments. Sample **4** has a sharper inflection point at low pressures and less steep adsorption at higher pressures as compared to sample **5**. These differences may be due to the difference in porosity between both samples, sample **4** being microporous and sample **5** combining micro- and mesoporosity. Note that NH₃ can, in principle, chemisorb to both the silanol and the vanadium sites (both V(V) and vanadyl). The two-cycle adsorption experiments do not unambiguously prove chemisorptions to the vanadyl centers. This is only clear from the EPR experiments.

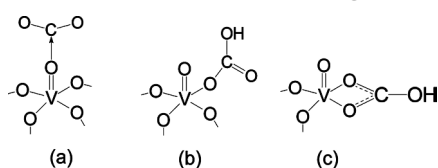
Discussion

The analysis of the phase memory times T_m of the VO(II) sites in the VS1-SBA15 samples as compared to the full-grown VS-1 shows a larger heterogeneity in the vanadyl sites for the former case. This can be related to our earlier observation that the vanadyl sites in VS-1 nanoparticles (in VS1-SBA15) are situated at the particle surface.³⁷ The local concentration of the vanadyl sites was found to be larger in full-grown VS-1 than in the VS1-SBA15 materials. These results thus imply that only a limited number of vanadyl centers is present on the VS-1 nanoparticle surface and that the increased local concentration in full-grown VS-1 stems from the aggregation of the nano particles (and hence approaching of the vanadyl surface centers) as the zeolite grows. The vanadyl centers in both full-grown VS-1 and VS1-SBA15 are oxidized to the EPR-silent V(V) upon calcination at 550°C. These vanadium centers are accessible to H₂ and can be reduced back to a V(IV) form. In agreement with an earlier observation of Prakash and Kevan,⁴⁴ we find that applying a calcination/reduction cycle to full-grown VS-1 leads to the observation of a single V(IV) center, whose EPR parameters are typical for vanadyl species and not for V⁴⁺ in a tetrahedral coordination (sample **4**). The observation of a single vanadyl site after calcination/reduction proves that the two vanadyl centers observed in full-grown VS-1 (sample **1**) are not due to vanadium species located at different framework sites, but are merely due to a difference in the water ligation of the vanadium.⁴⁴ Prakash and Kevan⁴⁴ compared the reduction of the vanadium sites after H₂ treatment and after CO treatment at 673 K. Because they found slight differences in the CW-EPR spectra of the resulting vanadyl centers, they assumed weak interaction of H₂ and CO with the vanadyl sites. The ¹H HYSCORE spectrum of sample **4** reveals a weak proton interaction (maximum coupling 3.5 MHz), which may indeed stem from a weak interaction with H₂ or H⁺. Reduction of V⁵⁺ will occur as follows



whereby the H⁺ will be stabilized on an oxide ion as a hydroxyl. This hydroxyl is not expected to be in the first coordination sphere. The observed interaction is indeed too weak to be ascribed to axially or equatorially ligating -OH fragments.⁴⁸ In this respect, it is interesting to note that the observed ¹H hyperfine interaction found for the vanadyl sites in calcined/reduced VS1-SBA15 (sample **5**) is smaller than that for sample **4**, indicating that a weaker (or no) interaction occurs between the H⁺ (or remaining H₂) and VO(II) in the former case. This points to the important role that the zeolite pores play in stabilizing the VO²⁺-H⁺ system (or VO²⁺-H₂ system). Indeed, in VS1-SBA15, the vanadyl sites are on the surface of the nanoparticles, while the vanadyl sites in VS-1 are located inside the zeolite cages, which leads to other boundary conditions. In the VS-1 case, the confinement of the H₂ molecule in the cage may lead to an increased interaction with the vanadyl site. The large accessibility of the vanadyl sites in VS1-SBA15 and their location on the nanoparticle surface are corroborated by the ammonia adsorption experiments (sample **6**). A clear equatorial binding of at least two NH₃ molecules was proven by the ¹⁴N HYSCORE analysis (Figure 4). The ¹⁴N hyperfine and nuclear quadrupole values are similar to those observed after ammonia adsorption to vanadium-exchanged ZSM-5, but contrast the ESEEM finding for ammonia treated dehydrated VS-1.⁴⁴ For the latter, ²H ESEEM indicated that only one NH₃ molecule was binding axially to the vanadyl site. In the ZSM-5 case, the vanadyl is known to be highly accessible due to the nature of the preparation. The current findings thus confirm that the vanadyl sites on the nanoparticles have a clearly different surrounding from the ones in the full-grown VS-1. The two-cycle NH₃ adsorption experiments show that chemisorption of NH₃ in calcined/reduced VS-1 and VS1-SBA15 is not limited to the low temperatures (4-15 K) used for EPR. The latter experiments, however, do not allow one to differentiate between NH₃ binding to silanol or vanadium sites. In contrast, the two-cycle CO₂ adsorption experiments show no evidence for chemisorption of CO₂ at 373 K neither to calcined/reduced VS-1 nor VS1-SBA15. These experiments show, however, a large difference in the CO₂ adsorption capacity of calcined/reduced VS-1 as compared to calcined/reduced VS1 SBA15 with increasing pressure of CO₂. Furthermore, the ¹³C HYSCORE experiments performed at 4 K revealed a clear binding of CO₂ to vanadyl in calcined/reduced VS-1 (sample **9**). To our knowledge, only one study has reported ¹³C spin Hamiltonian parameters of a $VO_2-O-^{13}C-O$ unit, the recent HYSCORE study of oxidation of CO cocatalyzed by Pd(0) and the H₅PV₂Mo₁₀O₄₀ polyoxometalate.⁵¹ In the latter work, the maximum observed ¹³C hyperfine value is 2.85 MHz. This resembles the parameters for C(1) (Table 4). The authors interpreted this hyperfine coupling in terms of ¹³CO interacting with an oxygen ligand equatorially bound to the vanadyl ($VO_2-O-^{13}C-O-H$), whereby the CO double bond is interacting with Pd.⁵¹ The location of the carbon nucleus was based on the orientation of the ¹³C hyperfine tensor, which was assumed to be purely dipolar in nature (a_{iso}) 0 MHz and V-C distance of ~0.24 nm. The presence of the activating Pd and the use of CO in ref 51 makes that the situation may not be fully comparable with the current case. Indeed, the ¹³C hyperfine value of C(2) is characterized by a large isotropic hyperfine.

SCHEME 1: Three Potential CO₂ Binding Schemes to the Vanadyl Sites



value (a_{iso}) (16.3 MHz), whereas the a_{iso} value (a_{iso}) ($A_1 + A_2 + A_3/3$) of C(1) is only ~ 0.9 MHz (Table 4). The isotropic hyperfine value of C(2) agrees with a spin density of 0.48% ($100a_{\text{iso}}/a_0$ with g_0) 3333.67 MHz⁵²) in the carbon s-orbital. In our recent work on vanadium incorporation in MCM-41, we observed a strong ^{29}Si interaction resulting from an equatorial V-O-Si segment.⁵³ The ^{29}Si hyperfine interaction agreed with $\sim 0.23\%$ s-orbital spin density. Similarly, the isotropic ^1H hyperfine value of water molecules equatorially ligated to vanadyl is found to correspond to 0.29-0.34% spin density.⁴⁸ The similarity with the spin density in the s-orbital of C(2) gives confidence to the assignment of C(2) to an equatorially bound CO_2 fragment (V-O-C). The protons of axially bound water in $[\text{VO}(\text{H}_2\text{O})_5]^{2+}$ exhibit a small isotropic hyperfine value (~ 0.5 MHz).⁴⁸ This indicates that C(1) is most probably due to an axially ligated CO_2 . Scheme 1a illustrates the axial binding of CO_2 , which may be facilitated by the basicity of the vanadyl oxygen.

The weak ^{13}C hyperfine interaction observed after CO_2 adsorption to calcined/reduced VS1-SBA15 (sample **10**) indicates only a weak interaction of CO_2 with the vanadyl sites on the VS-1 nanoparticles.

The different factors influencing carbon dioxide adsorption on zeolites have been reviewed by D. Bonenfant et al.⁵⁴ Temperature is known to play a crucial role in CO_2 adsorption. It was shown that the CO_2 adsorption capacity of silicalite-1 increases strongly, when lowering the temperature from 473 to 323 K.⁵⁵ When comparing the two-cycle adsorption experiments with the EPR measurements, we therefore have to keep in mind that the experiments have been done at completely different temperatures (two-cycle adsorption at 373 K, EPR at 4-15 K). In the case of such weak bonds as those encountered here, the adsorption-desorption equilibrium for CO_2 should shift drastically toward the desorption side when increasing temperature, which makes it difficult to monitor any covalent bonding at higher temperatures. In addition, two-cycle adsorption results display an effect related to all of the surface, whereas EPR only observes the local interactions at the fraction of vanadyl species, which form a minority.

The CO_2 adsorption capacity of pure SiO_2 materials, such as silicate-1 and SBA-15, was found to be low in comparison to metal-exchanged materials or ZSM-5 structures with a high Al/Si ratio.^{54,56} For low pressures of CO_2 , the uptake capacity of silicalite-1 was found to be approximately twice that of SBA-15 at 303 K.⁵⁶ This agrees with the diminished affinity for CO_2 in case of the VS1-SBA15 versus full-grown VS-1 measured with the two-cycle adsorption experiments.

Silicate-1 is known to be able to physisorb CO_2 and to chemisorb CO_2 through the formation of carbonate species,⁵⁵ probably by coordinating of CO_2 to terminal basic -SiOH groups or to basic oxygen ions.⁵⁷ Formation of carbonate centers was detected in silicalite-1 via FTIR at different temperatures.⁵⁵ Different binding modes involving framework oxygen and a cation were reported for oxides.⁵⁷ Carbonate species have been reported to be formed by reaction of CO_2 with surface oxide ions in vanadyl compounds.⁵⁸ Case (b) in Scheme 1 represents a CO_2 addition reaction toward one of the equatorial oxygens. In this case, the isotropic ^{13}C hyperfine will be small because the carbon nucleus will be out of the equatorial plane. It was shown theoretically (based on DFT computing) that rotation of the water protons out of the equatorial plane of pentaquovanadyl leads to a reduction of the isotropic coupling.⁵⁹ Case (c) in Scheme 1 shows a similar association of CO_2 with one of the equatorial oxygens, but now bidentate ligation is taking place. This case implies the presence of coordinative unsaturated vanadyl units prior to CO_2 admission, which may be due to defect sites. In this configuration, the ^{13}C nucleus is in the equatorial plane, which will lead to large a_{iso} values, as observed for C(2).

The difference between samples **9** and **10** in terms of binding of CO_2 (or carbonate) to the vanadyl center is surprising. While sample **9** manifests strong equatorial binding to the vanadyl site, only a weak interaction with CO_2 is found for the VO(II) centers in VS1-SBA15. In fact, because the VS-1 nanoparticles are small, the external surface where the uncondensed silanol groups are present is large versus the bulk volume. The vanadyl species are found to be mainly on the nanoparticle surface and are thus in a silanol-rich environment. These silanols can in principle react with CO_2 to form stable carbonates that can coordinate to the vanadyl. Nevertheless, the stronger ^{13}C hyperfine interactions are seen for full-grown VS-1 and not for VS1-SBA15. This indicates that the pore size plays an important role in the observed binding to vanadyl in VS-1. Indeed, in the preparation of samples **9** and **10**, low CO_2 pressures (25 mbar) were used. Studies on different zeolites have shown that, at low pressures, the density of the adsorbate is highest in the smaller pores.⁵⁴ The confinement of the CO_2 in the small zeolite pores where the vanadyl centers are located may lead to closer contact between the vanadyl sites and the CO_2 leading to binding (chemisorption) at low temperature. This is in contrast to the vanadyl centers that are surface-bound on the VS-1 nanoparticles in VS1-SBA15, the nanoparticles being inside the large meso-pores of SBA15 that are too big to trap CO_2 effectively. This is also corroborated by the difference in CO_2 uptake by the two samples. Furthermore, similarly our proton HYSORE data suggest a larger interaction between the vanadyl sites and H_2 (H^+) in full-grown VS-1 as discussed earlier.

The difference between the CO_2 binding in the two cases is then most probably caused by the fact that more CO_2 is brought in closer contact with the vanadyl sites in full-grown VS-1, rather than a difference in the carbonate formation upon CO_2 adsorption. Low surface basicity of the silica surface also has an influence. CO_2 is acidic and hence prefers to adsorb on basic sites of metal oxides. Although SBA-15 does not possess any strong Brønsted or Lewis acid sites, the silanol groups on the SBA-15 are known to be slightly acidic.⁶⁰

Conclusions

In this work, the behavior of VS1-SBA15 was studied for different treatments (aging, calcination/reduction cycle, gas adsorption) and compared to full-grown VS-1. The EPR experiments show that the surrounding of the VO(II) sites in both samples differs clearly. This is already obvious from the CW-EPR data. Further experiments showed that, when the samples are aged, the VO(II) centers are more mobile in the case of VS1-SBA15 than in the full-grown zeolite. A large variety in phase-memory times was found for the VS1-SBA15 samples linking back to the heterogeneity of the VO(II) centers. The T_m measurements for full-grown VS-1

show a homogeneous spread of the VO(II) centers. NH₃ chemisorbs on the VO(II) sites in both full-grown zeolite and VS1-SBA15 samples that underwent a calcination/ reduction cycle. This means that in both cases the VO(II) sites are accessible for NH₃ molecules. Chemisorption was found to occur both at low (4 K) and high (373 K) temperatures.

Where neither the calcined/reduced VS1-SBA15 nor the calcined/reduced VS-1 showed chemisorptions of CO₂ at 373 K, HYSCORE experiments at 4 K revealed the equatorial binding of ¹³CO₂ to VO(II) in VS-1. The ¹³C hyperfine values suggest that this occurs via a bidentate binding mode. In the case of VS1-SBA15, only weak ¹³C hyperfine interactions were found, which imply a weaker out-of-plane association of CO₂, such as CO₂ binding to the vanadyl oxygen. A clear impact was observed of the presence or absence of confinement effects on the interaction of both CO₂ and H₂ with vanadyl induced by the differences in the pore dimensions.

Acknowledgment. S.V.D., F.V., and P.C. acknowledge the Fund of Scientific Research-Flanders (FWO) for financial support. S.Z. thanks the University of Antwerp for Ph.D. funding through the NOI-BOF grant system. V.M. is a postdoctoral associate of the FWO-Flanders. M.C. acknowledges financial support through the DAMMONEU6 project. Financial support by FP6 INSIDE_PORes Network of Excellence NMP3-CT-2004-200895 is also acknowledged.

Supporting Information Available: (S1,S2) ESE-detected EPR and magnetic-field dependence of T_m for sample **1** and sample **3**; (S3) X-band matched HYSCORE of sample **4**; (S4) X-band CW-EPR spectrum of sample **6**; (S5) X-band matched HYSCORE of sample **6**; (S6-S9) X-band CW-EPR spectra of samples **7-10**; (S10) two-cycle adsorption measurements with CO₂ of samples **4** and **5** at 373 K; and (S11) two-cycle adsorption measurements with NH₃ of samples **4** and **5** at 373 K.

References and Notes

- (1) Soler-Illia, G. J.; Sanchez, C.; Lebeau, B.; Patarin, J. Chemical strategies to design textured materials: from microporous and mesoporous oxides to nanonetworks and hierarchical structures. *Chem. Rev.* **2002**, *102*, 4093–4138.
- (2) Taguchi, A.; Schu'th, F. Ordered mesoporous materials in catalysis. *Microporous Mesoporous Mater.* **2005**, *77*, 1–45.
- (3) Meynen, V.; Cool, P.; Vansant, E. F. Verified syntheses of mesoporous materials. *Microporous Mesoporous Mater.* **2009**, *125*, 170–223.
- (4) Meynen, V.; Cool, P.; Vansant, E. F. Synthesis of siliceous materials with micro- and mesoporosity. *Microporous Mesoporous Mater.* **2007**, *104*, 26–38.
- (5) Perez-Ramirez, J.; Christensen, C. H.; Egeblad, K.; Christensen, C. H.; Groen, J. C. Hierarchical zeolites: enhanced utilization of microporous crystals in catalysis by advances in materials design. *Chem. Soc. Rev.* **2008**, *37*, 2530–2542.
- (6) Zhao, D.; Feng, J.; Huo, Q.; Melosh, N.; Fredrickson, G. H.; Chmelka, B. F.; Stucky, G. D. Triblock copolymer syntheses of mesoporous silica with periodic 50 to 300 angstrom pores. *Science* **1998**, *279*, 548–552.
- (7) Kruk, M.; Jaroniec, M.; Ko, C. H.; Ryoo, R. Characterization of the porous structure of SBA-15. *Chem. Mater.* **2000**, *12*, 1961–1968.
- (8) Bennadja, Y.; Beaunier, P.; Margolese, D.; Davidson, A. Fine tuning of the interaction between Pluronic surfactants and silica walls in SBA-15 nanostructured materials. *Microporous Mesoporous Mater.* **2001**, *147*, 44–45.
- (9) Cassiers, K.; Linsse, T.; Mathieu, M.; Benjelloun, M.; Schrijne-makers, K.; Van Der Voort, P.; Cool, P.; Vansant, E. F. A detailed study of thermal, hydrothermal, and mechanical stabilities of a wide range of surfactant assembled mesoporous silicas. *Chem. Mater.* **2002**, *14*, 2317–2324.
- (10) Kim, J. M.; Stucky, G. D. Synthesis of highly ordered mesoporous silica materials using sodium silicate and amphiphilic block copolymers. *Chem. Commun.* **2000**, 1159–1160.
- (11) Kim, S. S.; Pauly, T. R.; Pinnavaia, T. J. Non-ionic surfactant assembly of ordered, very large pore molecular sieve silicas from water soluble silicates. *Chem. Commun.* **2000**, 1661–1662.
- (12) Joo, S. H.; Ryoo, R.; Kruk, M.; Jaroniec, M. Evidence for general nature of pore interconnectivity in 2-dimensional hexagonal mesoporous silicas prepared using block copolymer templates. *J. Phys. Chem. B* **2002**, *106*, 4640–4646.
- (13) Choi, M.; Heo, W.; Kleitz, F.; Ryoo, R. Facile synthesis of high quality mesoporous SBA-15 with enhanced control of the porous network connectivity and wall thickness. *Chem. Commun.* **2003**, 1340–1341.
- (14) Newalkar, B. L.; Komarneni, S. Simplified synthesis of micropore-free mesoporous silica, SBA-15, under microwave-hydrothermal conditions. *Chem. Commun.* **2002**, 1774–1775.
- (15) Van Der Voort, P.; Ravikovitch, P. I.; De Jong, K. P.; Neimark, A. V.; Janssen, A. H.; Benjelloun, M.; Van Bavel, E.; Cool, P.; Weckhuysen, B. M.; Vansant, E. F. Plugged hexagonal templated silica: a unique micro-and mesoporous composite material with internal silica nanocapsules. *Chem. Commun.* **2002**, 1010–1011.
- (16) Van Der Voort, P.; Ravikovitch, P. I.; De Jong, K. P.; Benjelloun, M.; Van Bavel, E.; Janssen, A. H.; Neimark, A. V.; Weckhuysen, B. M.; Vansant, E. F. A new templated ordered structure with combined micro-and mesopores and internal silica nanocapsules. *J. Phys. Chem. B* **2002**, *106*, 5873–5877.
- (17) Van Bavel, E.; Cool, P.; Aerts, K.; Vansant, E. F. Plugged hexagonal templated silica (PHTS): An in-depth study of the structural characteristics. *J. Phys. Chem. B* **2004**, *108*, 5263–5268.
- (18) Kruk, M.; Jaroniec, M.; Joo, S. H.; Ryoo, R. Characterization of regular and plugged SBA-15 silicas by using adsorption and inverse carbon replication and explanation of the plug formation mechanism. *J. Phys. Chem. B* **2003**, *107*, 2205–2213.
- (19) Celer, E. B.; Kruk, M.; Zuzek, J.; Jaroniec, M. Hydrothermal stability of SBA-15 and related ordered mesoporous silicas with plugged pores. *J. Mater. Chem.* **2006**, *16*, 2824–2833.
- (20) Lee, J.; Park, Y.; Kim, P.; Kim, H.; Yi, J. Preparation of NaCl-incorporated plugged mesoporous silica using a cost-effective precursor and applications to the hydrodechlorination of chlorinated hydrocarbons. *Chem. Mater.* **2004**, *14*, 1050–1056.
- (21) Janssen, A. H.; Van Der Voort, P.; Koster, A. J.; De Jong, K. P. A 3D-TEM study of the shape of mesopores in SBA-15 and modified SBA-15 materials. *Chem. Commun.* **2002**, 1632–1633.
- (22) Meynen, V.; Segura, Y.; Mertens, M.; Cool, P.; Vansant, E. F. Diffusion effects in SBA-15 and its plugged analogous by a deposition of metal-acetylacetonate complexes. *Microporous Mesoporous Mater.* **2005**, *85*, 119–128.
- (23) Van Bavel, E.; Meynen, V.; Cool, P.; Lebeau, K.; Vansant, E. F. Adsorption of hydrocarbons on mesoporous SBA-15 and PHTS materials. *Langmuir* **2005**, *21*, 2447–2453.
- (24) Kortunov, P.; Valiullin, R.; Ka'rrger, J.; Meynen, V.; Vansant, E. F. Transport Properties of Guest Molecules in Mesoporous SBA-15 Materials - A PFG NMR Study. *Diffus. Fundam.* **2005**, *2*, 95.195.2.

- (25) Meynen, V.; Cool, P.; Vansant, E. F.; Kortunov, P.; Grinberg, F.; Ka'rger, J.; Mertens, M.; Lebedev, O. I.; Van Tendeloo, G. Deposition of vanadium silicalite-1 nanoparticles on SBA-15 materials. Structural and transport characteristics of SBA-VS-15. *Microporous Mesoporous Mater.* **2007**, *99*, 14–22.
- (26) Cheneviere, Y.; Chieux, F.; Caps, V.; Tuel, A. Synthesis and catalytic properties of TS-1 with mesoporous/microporous hierarchical structures obtained in the presence of amphiphilic organosilanes. *J. Catal.* **2010**, *269*, 161–168.
- (27) Reichinger, M.; Schmidt, W.; Van den Berg, M. W. E.; Aerts, A.; Martens, J. A.; Kirschhock, C. E. A.; Gies, H.; Gru'ner, W. Alkene epoxidation with mesoporous materials assembled from TS-1 seeds - Is there a hierarchical pore system. *J. Catal.* **2010**, *269*, 367–375.
- (28) Trong-On, D.; Ungureanu, A.; Kaliaguine, S. TS-1 coated meso-cellular titano-silica foams as new catalysts for oxidation of bulky molecules. *Phys. Chem. Chem. Phys.* **2003**, *5*, 3534–3538.
- (29) Ungureanu, A.; Trong-On, D.; Dumitriu, E.; Kaliaguine, S. Hydroxylation of 1-naphthol by hydrogen peroxide over UL-TS-1 coated MCF. *Appl. Catal., A* **2003**, *245*, 203–223.
- (30) Shylesh, S.; Singh, A. P. Synthesis, characterization, and catalytic activity of vanadium-incorporated, -grafted, and -immobilized mesoporous MCM-41 in the oxidation of aromatics. *J. Catal.* **2004**, *228*, 333–346.
- (31) Capek, L.; Bulanek, R.; Adam, J.; Smolaková, L.; Sheng-Yang, H.; Cicmanec, P. Oxidative dehydrogenation of ethane over vanadium-based hexagonal mesoporous silica catalysts. *Catal. Today* **2009**, *141*, 282–287.
- (32) Takahara, I.; Saito, M.; Inaba, M.; Murata, K. Dehydrogenation of propane over a silica-supported vanadium oxide catalyst. *Catal. Lett.* **2005**, *102*, 201–205.
- (33) Anpo, M.; Higashimoto, S.; Matsuoka, M.; Zhanpeisov, N.; Shioya, Y.; Dzwigaj, S.; Che, M. The effect of the framework structure on the chemical properties of the vanadium oxide species incorporated in zeolites. *Catal. Today* **2003**, *78*, 211–217.
- (34) Meynen, V.; Beyers, E.; Cool, P.; Vansant, E. F.; Mertens, M.; Weyten, H.; Lebedev, O. I.; Van Tendeloo, G. Post-synthesis deposition of V-zeolitic nanoparticles in SBA-15. *Chem. Commun.* **2004**, 898–890.
- (35) Goldfarb, D. High field ENDOR as a characterization tool for functional sites in microporous materials. *Phys. Chem. Chem. Phys.* **2006**, *8*, 2325–2343.
- (36) Van Doorslaer, S.; Caretti, I.; Fallis, I. A.; Murphy, D. M. The power of electron paramagnetic resonance to study asymmetric homogeneous catalysts based on transition-metal complexes. *Coord. Chem. Rev.* **2009**, *253*, 2116–2130.
- (37) Chiesa, M.; Meynen, V.; Van Doorslaer, S.; Cool, P.; Vansant, E. Vanadium silicalite-1 nanoparticles deposition onto the mesoporous walls of SBA-15. Mechanistic insights from a combined EPR and Raman study. *J. Am. Chem. Soc.* **2006**, *128*, 8955–8963.
- (38) Han, Y.; Xiao, F.-S.; Wu, S.; Sun, Y.; Meng, X.; Li, D.; Lin, S.; Deng, F.; Ai, X. A novel method for incorporation of heteroatoms into the framework of ordered mesoporous silica materials synthesized in strong acidic media. *J. Phys. Chem. B* **2001**, *105*, 7963–7966.
- (39) Stevens, W. J. J.; Meynen, V.; Bruijn, E.; Lebedev, O. I.; Van Tendeloo, G.; Cool, P.; Vansant, E. F. Mesoporous material formed by acidic hydrothermal assembly of silicalite-1 precursor nanoparticles in the absence of meso-templates. *Microporous Mesoporous Mater.* **2008**, *110*, 77–85.
- (40) Stoll, S.; Schweiger, A. EasySpin, a comprehensive software package for spectral simulation and analysis in EPR. *J. Magn. Reson.* **2006**, *178*, 42–55.
- (41) Ho'fer, P.; Grupp, A.; Nebenfu'r, H.; Mehring, M. Hyperfine sublevel correlation (HYSCORE) spectroscopy - A 2D electron-spin-resonance investigation of the squaric acid radical. *Chem. Phys. Lett.* **1986**, *132*, 279–282.
- (42) Jeschke, G.; Rakhmatullin, R.; Schweiger, A. Sensitivity enhancement by matched microwave pulses in one- and two-dimensional electron spin echo envelope modulation spectroscopy. *J. Magn. Reson.* **1998**, *131*, 261–271.
- (43) Madi, Z. L.; Van Doorslaer, S.; Schweiger, A. Numerical simulation of one- and two-dimensional ESEEM experiments. *J. Magn. Reson.* **2002**, *154*, 187–191.
- (44) Prakash, A. M.; Kevan, L. Structure and adsorbate interactions of vanadium in a vanadium silicate (VS-1) molecular sieve. *J. Phys. Chem. B* **2000**, *104*, 6860–6868.
- (45) Atherton, N. M.; Shackleton, J. F. Proton ENDOR of $\text{VO}(\text{H}_2\text{O})_5^{2+}$ in $\text{Mg}(\text{NH}_4)_2(\text{SO}_4)_2 \cdot 6\text{H}_2\text{O}$. *Mol. Phys.* **1980**, *39*, 1471–1485.
- (46) Woodworth, J.; Bowman, M. K.; Larsen, S. C. Two-dimensional pulsed EPR studies of vanadium-exchanged ZSM-5. *J. Phys. Chem. B* **2004**, *108*, 16128–16134.
- (47) Chasteen, N. D. Vanadyl(IV) EPR Spin Probes: Inorganic and Biochemical Aspects. In *Biological Magnetic Resonance*; Berliner, L. J., Reuben, J., Eds.; Plenum: New York, 1981; Vol. 3, p 53.
- (48) Mustafi, D.; Makinen, M. W. ENDOR determined solvation structure of VO^{2+} in frozen solutions. *Inorg. Chem.* **1988**, *27*, 3360–3368.
- (49) Stoll, S.; Calle, C.; Mitrikas, G.; Schweiger, A. Peak suppression in ESEEM spectra of multinuclear spin systems. *J. Magn. Reson.* **2005**, *177*, 93–101.
- (50) Fukui, K.; Ohya-Nishiguchi, H.; Kamada, H. ^{14}N coupling parameters in oxovanadium(IV)-amine, -imine, and -isothiocyanate complexes studied by electron spin echo envelope modulation spectroscopy. *Inorg. Chem.* **1997**, *36*, 5518–5529.
- (51) Goldberg, H.; Kaminker, I.; Goldfarb, D.; Neumann, R. Oxidation of carbon monoxide cocatalyzed by palladium(0) and the $\text{H}_5\text{PV}_2\text{Mo}_{10}\text{O}_{40}$ polyoxometalate probed by electron paramagnetic resonance and aerobic catalysis. *Inorg. Chem.* **2009**, *48*, 7947–7952.
- (52) Fitzpatrick, J. A. J.; Manby, F. R.; Western, C. M. The interpretation of molecular magnetic hyperfine interactions. *J. Chem. Phys.* **2005**, *122*, 084312.
- (53) Zamani, S.; Meynen, V.; Hanu, A.-M.; Mertens, M.; Popovici, E.; Van Doorslaer, S.; Cool, P. Direct spectroscopic detection of framework-incorporated vanadium in mesoporous silica materials. *Phys. Chem. Chem. Phys.* **2009**, *11*, 5823–5832.
- (54) Bonenfant, D.; Kharoune, M.; Niquette, P.; Mimeault, M.; Hausler, R. Advances in principal factors influencing carbon dioxide adsorption on zeolites. *Sci. Technol. Adv. Mater.* **2008**, *9*, 013007.
- (55) Wirawan, S. K.; Creaser, D. CO_2 adsorption on silicalite-1 and cation exchanged ZSM-5 zeolites using a step change response methods. *Microporous Mesoporous Mater.* **2006**, *91*, 196–205.
- (56) Kno'fel, C.; Lutecki, M.; Martin, C.; Mertens, M.; Hornebecq, V.; Llewellyn, P. L. Green solvent extraction of a triblock copolymer from mesoporous silica: Application to the adsorption of carbon dioxide under static and dynamic conditions. *Microporous Mesoporous Mater.* **2010**, *128*, 26–33.
- (57) Lavalley, J. C. Infrared spectrometric studies of the surface basicity of metal oxides and zeolites using adsorbed probe molecules. *Catal. Today* **1996**, *27*, 377–401.
- (58) Puttock, S. J.; Rochester, C. H. Infrared study of the adsorption of carbon monoxide, carbon dioxide, acetic acid and acetic anhydride on the surface of anhydrous vanadyl pyrophosphate. *J. Chem. Soc., Faraday Trans. 1* **1986**, *82*, 3013–3018.
- (59) Larsen, S. C. DFT calculations of proton hyperfine coupling constants for $[\text{VO}(\text{H}_2\text{O})_5]^{2+}$: Comparison with proton ENDOR data. *J. Phys. Chem. A* **2001**, *105*, 8333–8338.
- (60) Srivastava, R.; Srinivas, D.; Ratnasamy, P. Sites for CO_2 activation over amine-functionalized mesoporous Ti(Al)-SBA-15 catalysts. *Microporous Mesoporous Mater.* **2006**, *20*, 314–326.